Yao, Tongtong; Hou, Nianjun; Gan, Juanjuan; Wang, Jun; Zhi, Xiaojing; Fan, Lijun; Gan, Tian; Zhao, Yicheng; Li, Yongdan

Enhanced activity and stability of $Sr_2FeMo_{0.65}Ni_{0.35}O_{6-\delta}$ anode for solid oxide fuel cells with Na doping

Published in:
Journal of Power Sources

DOI:
10.1016/j.jpowsour.2019.04.004

Published: 15/06/2019

Document Version
Peer-reviewed accepted author manuscript, also known as Final accepted manuscript or Post-print

Enhanced activity and stability of $Sr_2FeMo_{0.65}Ni_{0.35}O_{6-\delta}$ anode for solid oxide fuel cells with Na doping

Tongtong Yao[1,2], Nianjun Hou[1,2], Juanjuan Gan[1,2], Jun Wang[1,2], Xiaojing Zhi[1,2], Lijun Fan[1,2], Tian Gan[1,2], Yicheng Zhao[1,2*], Yongdan Li[1,2,3]

[1]State Key Laboratory of Chemical Engineering (Tianjin University), Tianjin Key Laboratory of Applied Catalysis Science and Technology, School of Chemical Engineering, Tianjin University, Tianjin 300072, China

[2]Collaborative Innovation Center of Chemical Science and Engineering (Tianjin), Tianjin, 300072, China

[3]Department of Chemical and Metallurgical Engineering, Aalto University, Kemistintie 1, FI-00076 Aalto, Finland

Abstract

$Sr_{2-x}Na_xFeMo_{0.65}Ni_{0.35}O_{6-\delta}$ is synthesized as an anode material for solid oxide fuel cells. The effects of Na on the crystalline phase and electrical properties are investigated. The main perovskite phase changes into a Ruddlesden-Popper structure after reduction when x is less than 0.1, while the material with a higher amount of Na keeps the perovskite structure. $FeNi_x$ alloy nanoparticles are exsolved during reduction, in which the content of Ni increases with the rise of Na amount. The surface oxygen vacancy concentration is also influenced by the doping of Na, and the highest value is reached when x is 0.1. $Sr_{1.9}Na_{0.1}FeMo_{0.65}Ni_{0.35}O_{6-\delta}$ anode exhibits the highest activity, and a single cell supported by a 300-μm-thick $La_{0.8}Sr_{0.2}Ga_{0.8}Mg_{0.2}O_{3-\delta}$ electrolyte layer shows maximum power densities of 1495 and 627 mW cm^{-2} at 850 °C with H_2 and wet CH_4

*Corresponding author. Email: zhaoyicheng@tju.edu.cn; Tel: +86-22-27405613; Fax: +86-22-27405243 (Y. Zhao)

as fuels, respectively. The coking resistance of the anode is also improved with Na doping.

Keywords: Anode; Solid oxide fuel cell; Double perovskite; Methane; Sodium doping

1. Introduction

Solid oxide fuel cells (SOFCs) are promising energy converting devices with high efficiency and low emissions, which can be used for both stationary and portable power generation [1, 2]. Anodes catalyzing electrochemical oxidation of fuels such as H_2 and hydrocarbons are key components in SOFCs, which require high activity and sufficient ionic and electronic conductivities [3-5]. Until today, the most mature anode material applied practically is still nickel-based cermet such as Ni/yttrium-stabilized zirconia. Though Ni shows excellent catalytic activity and adequate electronic conductivity, many serious problems hinder its long-term reliability, such as low redox stability, agglomeration at high temperature and coking in hydrocarbon fuels [6, 7]. In the last two decades, oxide materials with various structures, such as fluorite (AO_2, e.g. $Ce_{0.6}Gd_{0.4}O_{1.8}$ [8]), pyrochlore ($A_2B_2O_7$, e.g. $Gd_2Ti_{1.4}Mo_{0.6}O_7$ [9]), rutile (AO_2, e.g. $Ti_{0.8}Cr_{0.1}Nb_{0.1}O_2$ [10]) and perovskite (ABO_3), in which perovskite anodes have attracted the most attention.

Perovskite oxides exhibit a high structural flexibility with a wide non-stoichiometric window, facilitating the optimization of their electrical and catalytic properties, which are highly influenced by the metal ions in A and B sites, with appropriate substitution [11-14]. Single perovskite oxides stable in reducing anode atmospheres generally have early transition metals in their B sites, such as $La_{0.75}Sr_{0.25}Cr_{0.5}Mn_{0.5}O_3$ [15], $La_{0.4}Sr_{0.4}TiO_3$ [16] and $La_{0.6}Sr_{0.4}VO_3$ [17], which exhibit moderate electrical conductivities but insufficient catalytic activities. In 2006, Huang et al. [3] reported a double-perovskite anode material $Sr_2MgMoO_{6-\delta}$ with a high

electrochemical oxidation activity. Maximum power densities (P_{max}) of 838 and 438 mW cm^{-2} were achieved by a single cell supported by a 300-μm-thick $La_{0.8}Sr_{0.2}Ga_{0.83}Mg_{0.17}O_{2.815}$ electrolyte layer at 800 °C with H_2 and CH_4 as fuels, respectively. $Sr_2Fe_{2-x}Mo_xO_{6-\delta}$ with a similar structure also shows adequate activity and high resistance to coking with CH_4 and CH_3OH as fuels [18, 19]. In 2015, Sengodan et al. [20] developed a layered double perovskite $PrBaMn_2O_{5+\delta}$ anode which showed promising performance with H_2 and C_3H_8 as fuels but low activity with CH_4 fuel.

In a reducing atmosphere, highly reducible transition metals such as Ni and Co in B sites of perovskite oxides tend to segregate on the surface as metallic nanoparticles with excellent activity and stability, providing a new strategy for the design of anode materials [21, 22]. The exsolution of Ni nanoparticles with a high coking resistance is reported from $La_{0.4}Sr_{0.4}Ni_{0.03}Ti_{0.97}O_{3-\delta}$ [23]. Yang et al. [24, 25] used a perovskite material $Pr_{0.4}Sr_{0.6}Co_{0.2}Fe_{0.7}Nb_{0.1}O_{3-\delta}$ as the anode, which changed to a Ruddlesden–Popper (RP) $Pr_{0.8}Sr_{1.2}(CoFe)_{0.8}Nb_{0.2}O_{4+\delta}$ structure with homogenously dispersed CoFe nanoparticles on the surface after reduction. Du et al. [26] substituted Mo in $Sr_2FeMoO_{6-\delta}$ partially with Ni, and the exsolved $FeNi_3$ alloy particles showed a high catalytic activity. A single cell with a 300-μm-thick $La_{0.8}Sr_{0.2}Ga_{0.83}Mg_{0.17}O_{2.815}$ electrolyte exhibited P_{max} of 960 and 500 mW cm^{-2} at 850 °C with wet H_2 and wet CH_4 as fuels, respectively. Sengodan et al. [27] investigated the co-segregation of Co, Ni and Fe from doped $PrBaMn_2O_{5+\delta}$ anode, and the P_{max} of a single cell with that anode reached 330 mW cm^{-2} at 800 °C with C_3H_8 fuel.

The electrical properties of perovskite oxides can be modified by doping alkali

metal ions in their A sites. The electronic and ionic conductivities of $SrFeO_{3-\delta}$ as a cathode material for SOFCs are both improved in air by partial substitution of K [28, 29]. However, that strategy is rarely used to design anode materials for SOFCs. Xiao et al. [13] reported an improved activity of $SrTi_{0.8}Nb_{0.2}O_3$ for H_2 electrochemical oxidation with the doping of Na and K, which was mainly attributed to the increase of oxygen vacancies. Meanwhile, the non-stoichiometry at A sites in perovskite oxides shows a significant influence on the surface exsolution of B-site metals [30]. In this work, Na is doped in the A sites of $Sr_2FeMo_{0.65}Ni_{0.35}O_{6-\delta}$ (SFMN). The effects of Na on the crystalline phase, exsolution of transition metals in the B sites and electrochemical properties of SFMN as an anode material with H_2 and CH_4 as fuels have been investigated.

2. Experimental

2.1. Anode powder preparation

$Sr_{2-x}Na_xFeMo_{0.65}Ni_{0.35}O_{6-\delta}$ (SNa_xFMN, x = 0, 0.05, 0.1, 0.2) powders were prepared through a citric nitrate combustion method [26, 31-33]. Stoichiometric $Sr(NO_3)_2$ (99.5%, Aladdin, China), $NaNO_3$ (≥ 99.0%, Guangfu fine chemical, Ltd., China), $Fe(NO_3)_3 \cdot 9H_2O$ (99.99%, Aladdin, China), $(NH_4)_6Mo_7O_{24} \cdot 4H_2O$ (99%, Aladdin, China) and $Ni(NO_3)_2 \cdot 6H_2O$ (99%, Adamas Reagent Co., Ltd., China) were dissolved in deionized water with a total metal cation concentration of 0.5 mol L^{-1}. Then citric acid (≥ 99.5%, Aladdin, China) was added to the solution with a concentration of 1 mol L^{-1}. The pH value of the solution was adjusted to 4 with the addition of ammonium hydroxide [26]. The solution was heated at 80 °C and formed gel. The gel

was slowly decomposed at 300 °C, and then calcined in air at 800 °C for 6 h to remove all the organic residues. The obtained powder was then pressed into pellets and sintered at 1200 ºC in air for 10 h to form the double-perovskite structure, which were then ground into fine powder. For characterization, the anode powders were reduced at 850 ºC in H_2 for 10 h.

2.2. Characterization

The oxygen vacancy concentrations in the anode powders before reduction were measured through iodometry with $Na_2S_2O_3$ (Alfa Aesar, 0.01 N standardized solution) and KI (≥ 99.0%, Tianjin Yuanli, China) [12, 14]. X-ray diffraction (XRD) patterns of the anode powders before and after reduction were recorded at a scanning rate of 1.2° min^{-1} with a D8 Focus diffractometer (Bruker Corp., Germany), Cu-Kα radiation, 40 kV and 200 mA, at room temperature. The morphology of the reduced powders was studied with a scanning electron microscope (SEM, S-4800, Hitachi) and a transmission electron microscope (TEM, JEM-2100F, JEOL). The surface property of the reduced powders was studied with X-ray photoelectron spectroscopy (XPS, 250xi, Thermo ESCALAB). All spectra were referenced to the C 1s binding energy of 284.8 eV. To compare the coking resistance between different anodes, the reduced powders were treated in wet CH_4 (~3% H_2O) at 850 ºC for 5 h, and the amounts of carbon deposition were measured with a thermogravimetric analyzer (TGA, STA449 F3, Netzsch) in air from 250 to 1000 ºC at a heating rate of 5 ºC min^{-1}.

2.3. Single cell fabrication and test

The single cells were supported by $La_{0.8}Sr_{0.2}Ga_{0.8}Mg_{0.2}O_{3-\delta}$ (LSGM) electrolyte

layers. LSGM powder (Fuel cell materials Co., USA) was pressed under 200 MPa into pellets with a thickness of 300 μm, and then sintered in air at 1450 °C for 20 h. $Ba_{0.5}Sr_{0.5}Co_{0.8}Fe_{0.2}O_{3-\delta}$ (BSCF) and $La_{0.4}Ce_{0.6}O_{2-\delta}$ (LDC) were used as cathode and anode interlayer materials, respectively, and the detailed preparation procedures could be found in other works [34-36]. SNa_xFMN, LDC and BSCF were made into slurries with a binder (V006, Heraeus Ltd.), respectively. LDC slurry was screen-printed on one side of the electrolyte layer and then sintered at 1400 ºC in air for 2 h. SNa_xFMN slurry was subsequently coated on the LDC layer, followed by sintering at 1150 ºC in air for 2 h. Finally, BSCF slurry was printed on the other side of the LSGM layer and sintered at 1000 ºC in air for 1 h. The effective electrode area was 0.50 cm^2. Ag paste was coated on both electrodes as current collector. Symmetrical cells with various anode materials were prepared via a similar procedure with LSGM electrolyte and LDC interlayers.

The single cells were tested in a homemade stainless reactor with H_2 and wet CH_4 (50 ml min^{-1}, STP) as fuels and O_2 (35 ml min^{-1}, STP) as oxidant. The anode was reduced in H_2 at 850 ºC for 2 h before the test. Current-voltage (*I-V*) and current-power density (*I-P*) curves of the cells were recorded with an electrochemical workstation (VersaSTAT 3, Ametek) in 750-850 ºC. The electrochemical impedance spectra (EIS) of the symmetrical cells were also measured with the workstation from 10^5 Hz to 10^{-2} Hz with an amplitude of 10 mV.

3. Results and Discussion

3.1. Characterization

The oxygen vacancy concertation (δ) of SFMN, $SNa_{0.05}FMN$, $SNa_{0.1}FMN$ and $SNa_{0.2}FMN$ before reduction determined with iodometry are 0.12, 0.15, 0.21 and 0.26, respectively. The partial substitution of Sr^{2+} by Na^{+} introduces more oxygen vacancies for charge compensation.

SFMN shows a pure double-perovskite structure similar to Sr_2FeMoO_6 (JCPDS #70-4093, Fig. 1a), which is in accordance with the result reported in a previous work [26]. The XRD refinement result shows that SFMN has a tetragonal structure (space group *I*4/*m*) with an average lattice volume of 241.56 $Å^3$ (Fig. S1a, Table S1). The radius of Na^{+} (1.39 Å, 12 coordination) is smaller than that of Sr^{2+} (1.44 Å, 12 coordination) [37], and the doping of Na should lead to the shrinkage of the unit cell. However, Table S1 shows a slight lattice expansion with the increase of the Na content, which can be explained by the decrease of lattice oxygen that weakens the metal-oxygen bonds [11, 33]. When the content of Na reaches 0.1, a weak peak corresponding to $SrMoO_4$ (JCPDS #85-0809) appears, which becomes more obvious in the result of $SNa_{0.2}FMN$. Another impure peak of NiO (JCPDS #71-1179) is also observed in $SNa_{0.2}FMN$. The replacement of Sr^{2+} with Na^{+} results in the reduction of the tolerance factor of the perovskite structure, resulting in the surface segregation of B-site metal ions as impure phases.

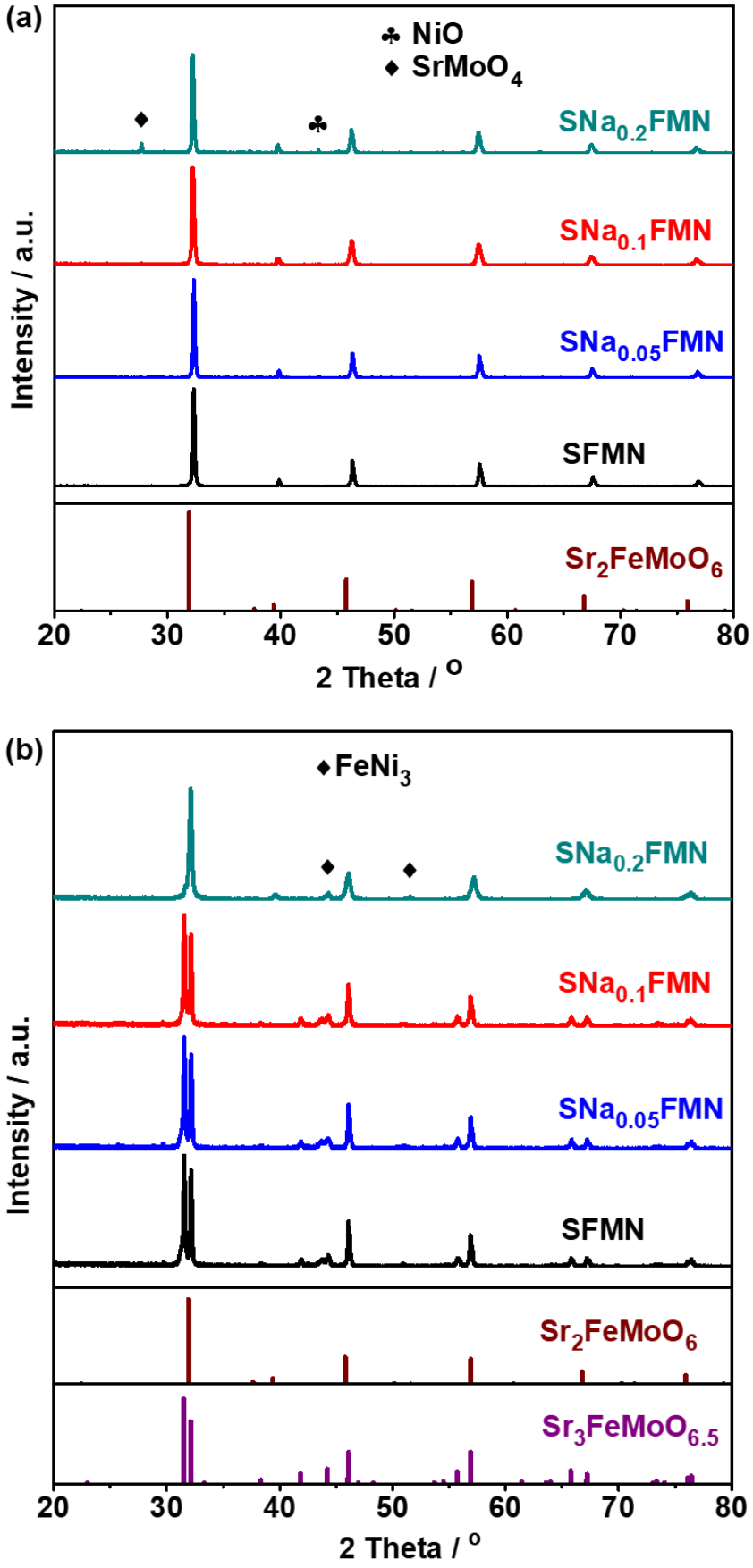

Fig. 1. XRD pattern of anode powders (a) before and (b) after reduction.

After reduction, the perovskite structure transforms into a RP phase similar to $Sr_3FeMoO_{6.5}$ (JCPDS #52-1715) with the exsolution of $FeNi_3$ alloy (JCPDS # 38-0419) when the content of Na is less than 0.1 (Fig. 1b) [26]. The loss of lattice oxygen and the exsolution of B-site transition metal ions lead to the decomposition of the perovskite and the formation of the Sr-rich new phase. Though $SNa_{0.2}FMN$ shows an unstable structure in the oxidation atmosphere with the formation of $SrMoO_4$ and NiO phases, it keeps a perovskite bulk phase with $FeNi_3$ alloy after reduction. $SrMoO_4$ and NiO are readily reduced, and the re-dissolution of the transition metal ions in the bulk phase contributes to the maintenance of the perovskite phase.

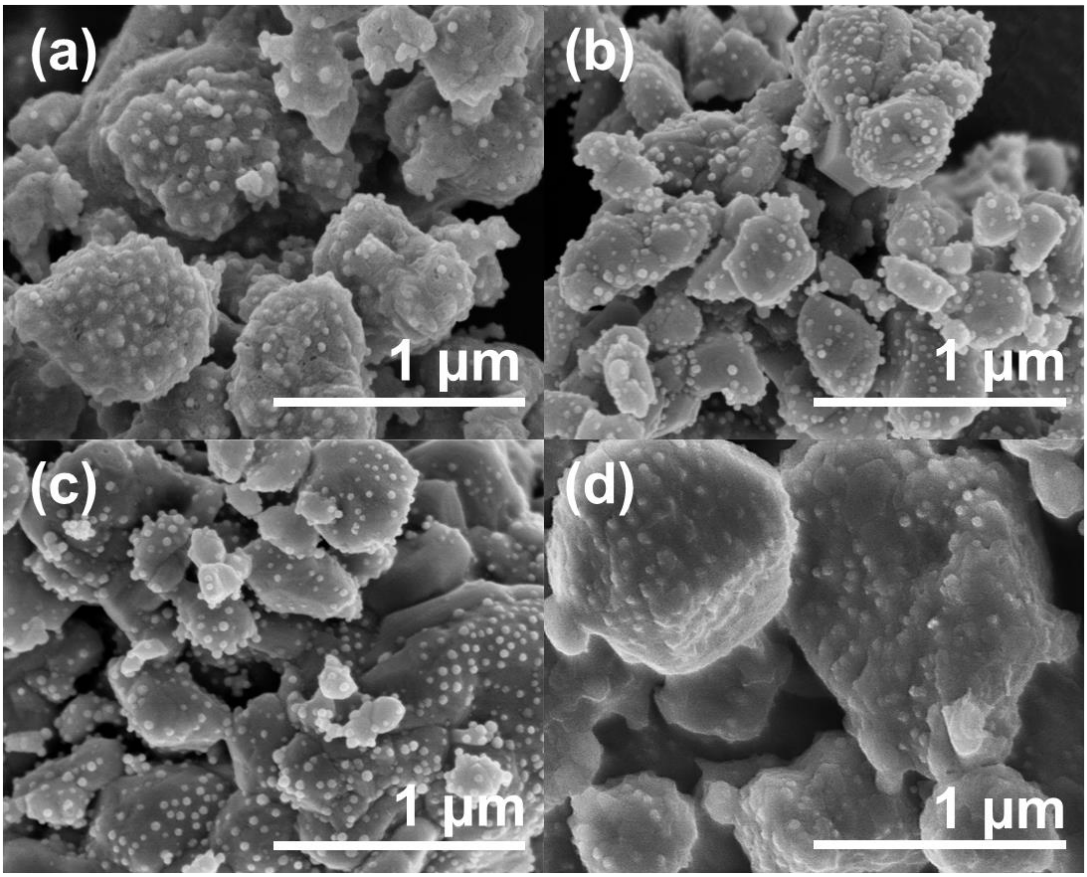

Fig. 2. SEM micrographs of anode powders after reduction. (a) SFMN; (b) $SNa_{0.05}FMN$; (c) $SNa_{0.1}FMN$; (d) $SNa_{0.2}FMN$.

The anode powders after reduction are composed of agglomerations with diameters of several hundred nanometers (Fig. 2). Nanoparticles with sizes of 10-30 nm distribute uniformly on the surface of the agglomerations. The TEM image of a nanoparticle (Fig. 3) on $SNa_{0.1}FMN$ reveals lattice spaces of 0.208 and 0.256 nm, which match (1 1 1) and (1 1 0) crystal planes of $FeNi_3$ alloy, respectively, proving that $FeNi_3$ alloy exsolves from the bulk phase as nanoparticles.

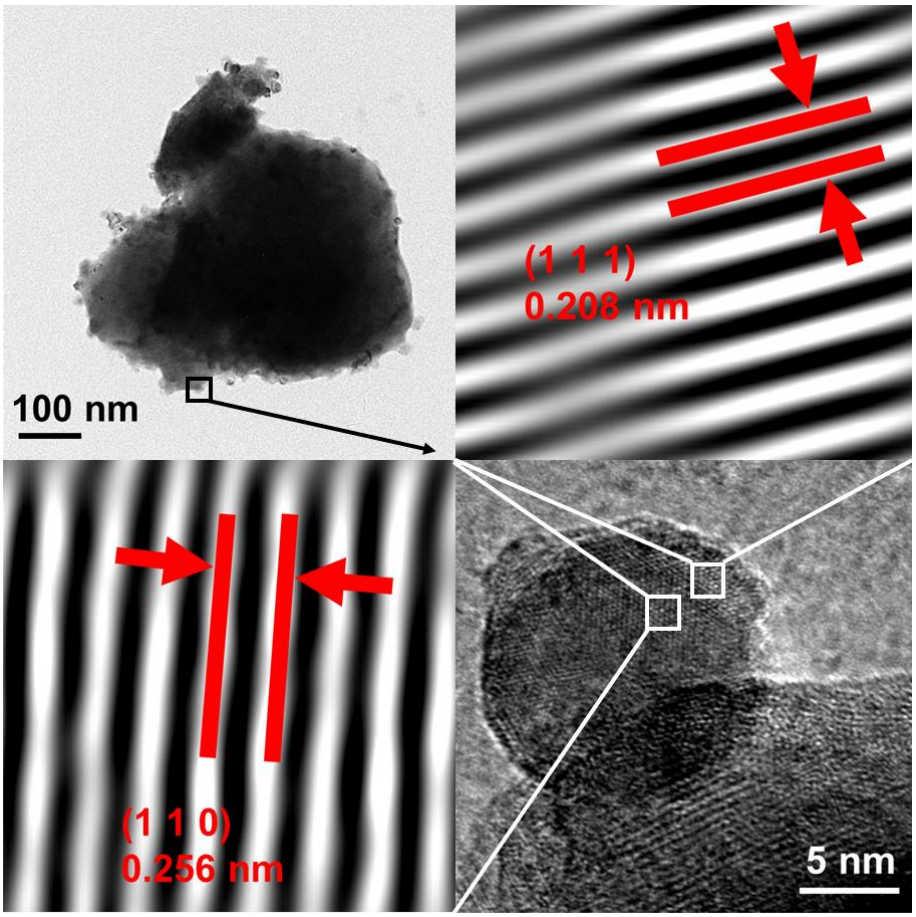

Fig. 3. TEM images of $SNa_{0.1}FMN$ powder after reduction.

The deconvolution of Ni-$2p_{3/2}$ core-level spectrum of reduced $SNa_{0.1}FMN$ is shown in Fig. 4. The peak at 852.3 eV corresponds to Ni^0, and those at 854.3 and 855.6 eV belong to Ni^{2+}. Fe^0 with the peak at 706.5 eV, Fe^{2+} with the peaks at 709.9/723.6 eV and Fe^{3+} with the peaks at 711.2/725.0 eV can be observed in the Fe-2p core-level spectrum. Mo-3d spectrum shows mixed valence states of Mo^{5+} and Mo^{6+} on the surface of reduced $SNa_{0.1}FMN$ with binding energies of 232.0/235.1 and 232.3/235.4 eV, respectively. O-1s spectrum is deconvoluted into three peaks at 529.5, 531.3 and 533.5 eV, corresponding to lattice oxygen, adsorbed oxygen and oxygen in water adsorbed, respectively. The XPS results of other reduced anode powders are shown in Fig. S2.

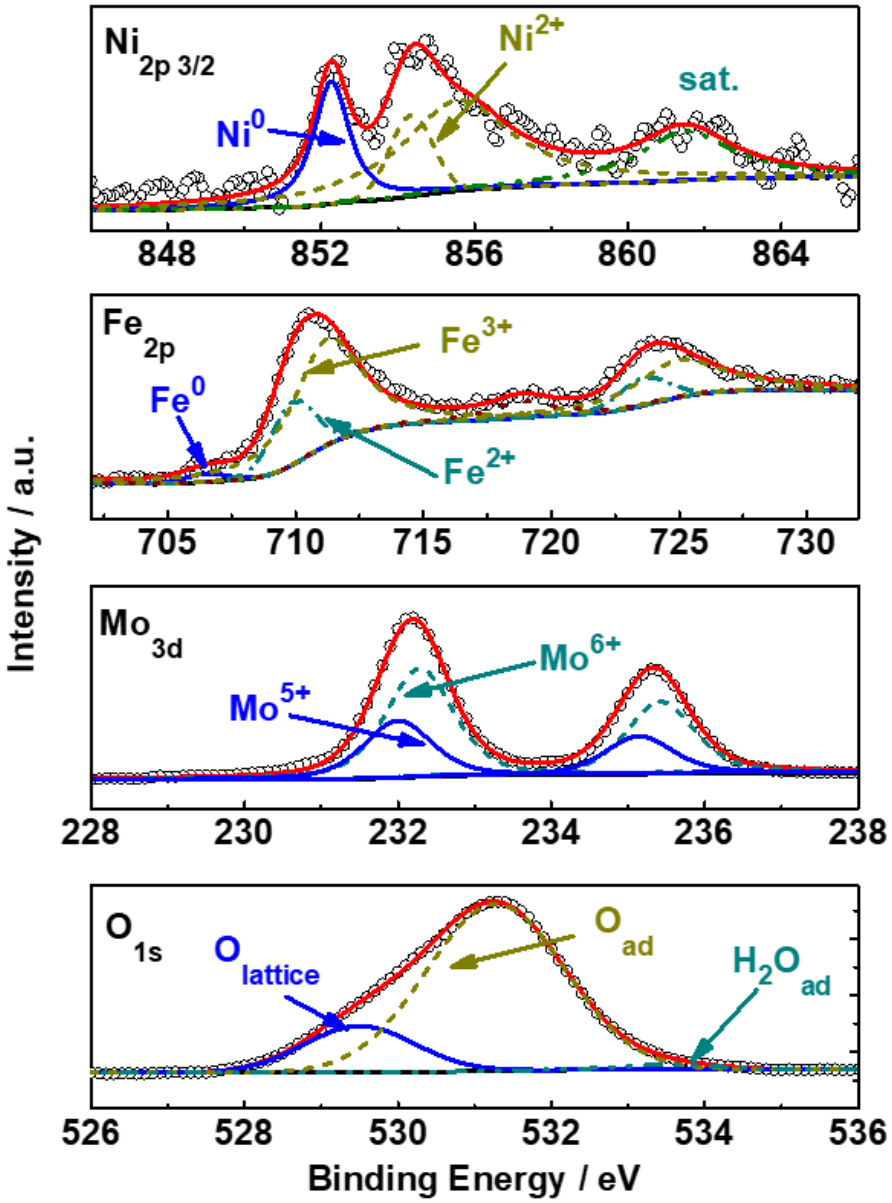

Fig. 4. XPS spectra of reduced $SNa_{0.1}FMN$ anode powder.

With the increase of Na content, less Fe is exsolved on the surface, while the content of Fe^{3+} in the bulk phase rises gradually (Table 1). The increase of the average valence state of Fe contributes to the neutralization of the negative charges introduced by Na^{+} substitution. The exsolution of metallic Ni shows no obvious relationship with the doping of Na. Nevertheless, the content of Ni in the exsolved nanoparticles

increases with the rise of the amount of Na. Based on the XPS results (Table 1), the compositions of nanoparticles exsolved from SFMN, $SNa_{0.05}FMN$ $SNa_{0.1}FMN$ and $SNa_{0.2}FMN$ are approximately $FeNi_{1.18}$, $FeNi_{2.78}$, $FeNi_{3.35}$ and $FeNi_{4.33}$, respectively. The amount of Mo^{5+} also goes up when the content of Na becomes higher, resulting in a higher electronic conductivity since the electron in the 4d orbital of Mo^{5+} ($4d^1$), which is not in Mo^{6+} ($4d^0$), acts as an electron charge carrier [38]. It is worth noting that the addition of Na results in an increase of Fe valence but a decrease of Mo valence, which is probably due to the formation of Fe^{3+}/Mo^{5+} redox couples [32]. With the increase of Na content from 0 to 0.1, the amounts of oxygen and water adsorbed both increase, implying a higher concentration of surface oxygen vacancies at a higher temperature, which is similar to the trend of oxygen vacancy amount in the anode powders before reduction determined with iodometry. However, a significant growth of lattice oxygen amount is observed when the content of Na reaches 0.2.

Table 1. Percentages of Fe, Ni, Mo and O in various valence states on the surface of reduced powders obtained from XPS spectra (%).

Samples	Fe			Ni		Mo		O		
	Fe^0	Fe^{2+}	Fe^{3+}	Ni^0	Ni^{2+}	Mo^{5+}	Mo^{6+}	$O_{lattice}$	O_{ad}	H_2O_{ad}
SFMN	8.20	25.80	66.00	27.65	72.35	28.69	71.31	21.98	74.18	3.84
$SNa_{0.05}FMN$	3.07	25.18	71.75	24.35	75.65	32.20	67.80	18.42	78.34	3.24
$SNa_{0.1}FMN$	2.64	21.38	75.98	25.24	74.76	34.52	65.48	17.87	80.33	1.81
$SNa_{0.2}FMN$	2.56	20.59	76.85	31.66	68.34	38.06	61.94	49.64	48.37	1.99

3.2. Anode performance in H_2

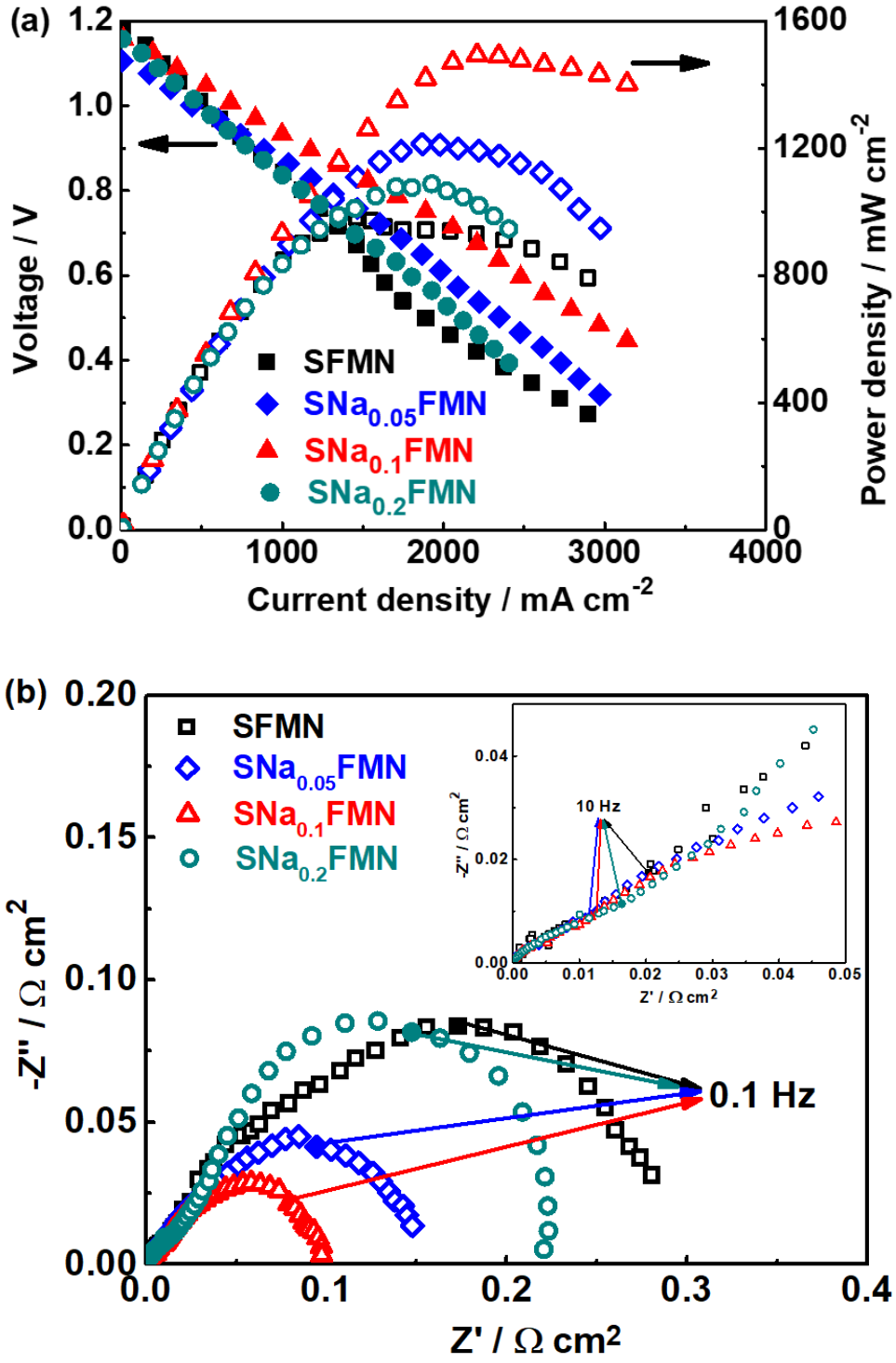

Fig. 5. (a) *I-V* and *I-P* curves of the single cells and (b) impedance spectra of the symmetrical cells with various anodes at 850 °C with H_2 as fuel.

The porous anode layer and LDC interlayer are 40 and 15-μm-thick, respectively (Fig. S3). The interlayer attaches closely to the dense LSGM electrolyte layer with a distinct interface. The open circuit voltages (OCVs) of the single cells with H_2 as fuel are in the range of 1.1-1.2 V at 850 ºC (Fig. 5a), indicating that there is negligible gas or electronic leakage through the dense electrolyte membrane. The P_{max} of the cell with the SFMN anode is 982 mW cm^{-2}, which is close to the value reported by Du et al. [26]. A remarkable improvement of the P_{max} is observed with the doping of Na in the anode, and the highest value of 1495 mW cm^{-2} is obtained by the cell with $SNa_{0.1}FMN$ as the anode. A further increase of Na content leads to a decrease of cell performance. The P_{max} of the $SNa_{0.1}FMN$ cell decreases to 1000 and 600 mW cm^{-2} at 800 and 750 ºC, respectively (Fig. S4).

The effects of Na content on the electrochemical performance of the anodes can be investigated based on the EIS results of the symmetrical cells (Fig. 5b). Ohmic resistances of the cells have been deducted from the results for a better comparison. The arcs corresponding to the anode polarization resistances (R_p) can be roughly divided into two parts, one in the high frequency region reflecting the charge transfer processes, and the other in the low frequency region mainly attributed to the surface processes including adsorption and surface diffusion. The mass transfer process, which is often observed in the low frequency region, is not obvious because hydrogen diffuses rapidly in the porous anode layer at 850 ºC. That is also proved by the almost constant slopes of the *I-V* curves in Fig. 5a.

Though it has been reported that Fe^{3+}/Mo^{5+} couples facilitate anode

electrochemical reaction [32, 39], no significant improvement on charge transfer is shown with the doping of Na. Conversely, the $SNa_{0.2}FMN$ anode with the most Fe^{3+}/Mo^{5+} couples shows the largest R_p in the high frequency region due to its lowest oxygen vacancy concentration. R_p of the anode mainly changes in the low frequency region. SFMN without doping exhibits the largest resistance of the surface processes. With a similar trend to the cell performance, the surface processes on the anode is greatly accelerated with the doping of Na, and $SNa_{0.1}FMN$ shows the lowest R_p. We propose that the surface processes on the anode are mainly affected in the following two ways:

(1) The dissociative adsorption of H_2 and spillover on the surface $FeNi_x$ nanoparticles. H_2 is moderately adsorbed on metallic Ni^0 ($3d^8$) due to the bonding between the electron in H atom and the hole in the 3d orbital of Ni [40], resulting in a high catalytic activity of Ni for H_2 dissociation. With more holes in its 3d orbital, Fe^0 ($3d^6$) shows a stronger adsorption of H_2 [41]. Therefore, H_2 is adsorbed strongly by $FeNi_{1.18}$ nanoparticles on the surface of SFMN, which hinders its spillover to the neighboring oxide for further reaction. The content of Fe in the nanoparticles decreases with the doping of Na, bringing about a proper adsorbing strength of H_2 which facilitates the overall rate of the adsorption and spillover of H species.

(2) The diffusion of active oxygen through surface oxygen vacancies. It is widely accepted that the surface oxygen vacancy concentration of oxide catalysts has a significant influence on their activity for oxidation reactions. As mentioned above, the increase of Na content from 0 to 0.1 brings about more surface oxygen vacancies (Table

1), promoting the electrochemical oxidation of surface H species. Nonetheless, the surface oxygen vacancies reduce dramatically on $SNa_{0.2}FMN$, which shows a higher R_p.

3.3. Anode performance in wet CH_4

Fig. 6 shows the XRD patterns of the anode powders exposed in wet CH_4 at 850 ^oC for 5 h after reduction. The Sr-riched RP phase in the reduced SFMN disappears, and the main perovskite structure is reformed due to the higher P_{O2} in wet CH_4 compared with that in dry H_2. Beside the perovskite and $FeNi_3$ alloy phases, a variety of impure phases, such as $Sr_2Fe_2O_5$ (JCPDS #89-8670), $SrCO_3$ (JCPDS #84-1778), $SrMoO_4$ and NiO form during the phase transition. With the doping of Na, $Sr_2Fe_2O_5$ and $SrCO_3$ phases disappear gradually, while $SrMoO_4$ and NiO remain in all of the samples. Though the RP phase of $SNa_{0.1}FMN$ transforms into a perovskite structure, the concentration of surface oxygen vacancies does not change obviously, which is still much higher than that in $SNa_{0.2}FMN$ (Fig. S5).

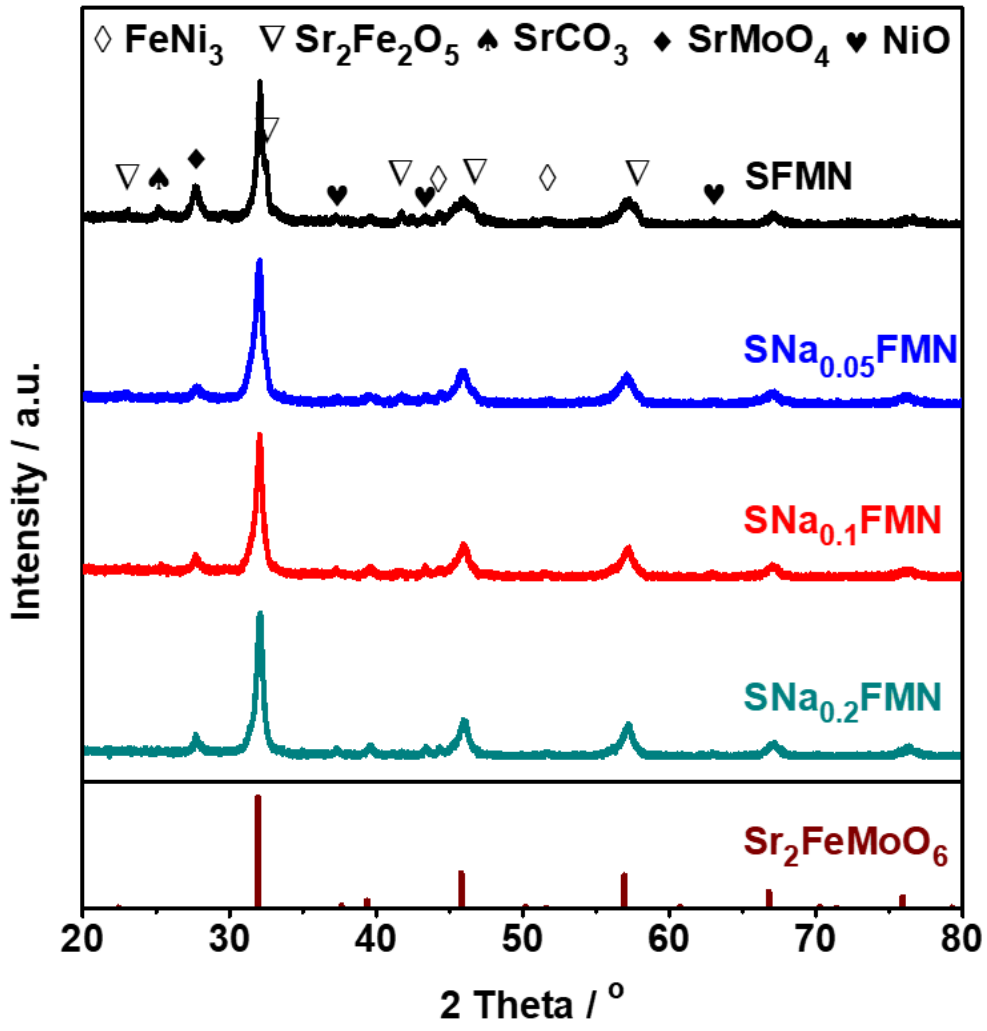

Fig. 6. XRD patterns of various anode powders exposed in wet CH_4 after reduction.

It is widely accepted that the coking resistance of oxides can be enhanced by alkali metal dopants [42, 43], which is proved by the TGA results of the anode powders after carbon deposition (Fig. 7). A rapid weight decrease is observed in the curve of SFMN with a total loss of about 6% when the temperature rises from 400 to 850 °C, corresponding to the oxidation of carbon. The weight loss above 850 °C is probably due to the gradual decomposition of $SrCO_3$ [44]. The amount of deposited carbon is reduced remarkably with the doping of Na. The weight losses of $SNa_{0.05}FMN$ and $SNa_{0.1}FMN$

are around 1% when the temperature reaches 1000 °C, and $SNa_{0.2}FMN$ shows the highest resistance to coking.

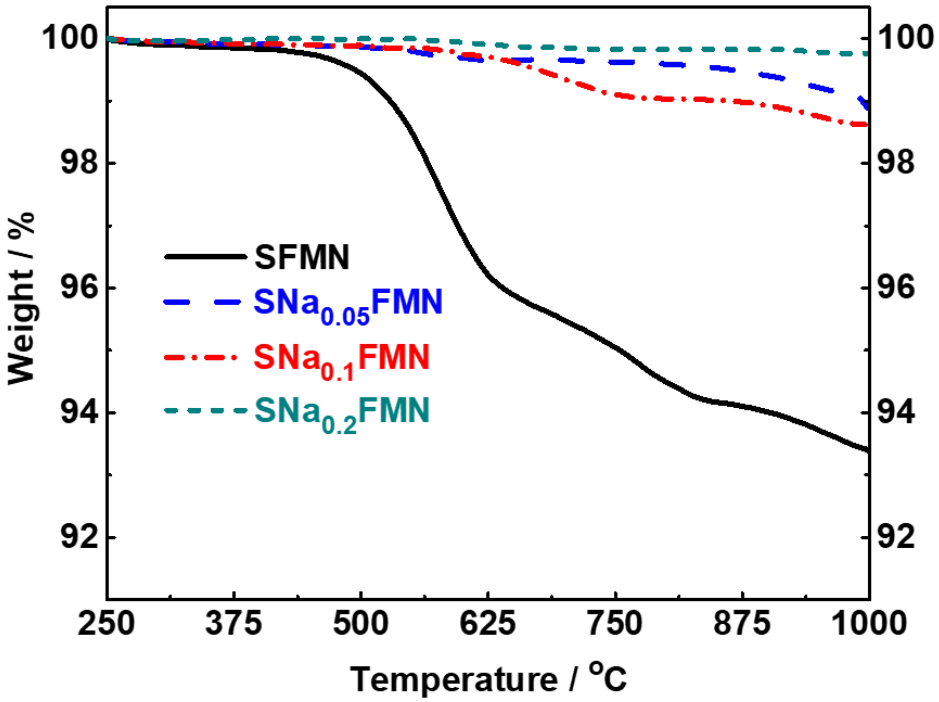

Fig. 7. TGA curves of various anode powders in air after carbon deposition.

The single cell with SFMN as the anode shows the lowest OCV of 0.90 V at 850 °C using wet CH_4 as fuel (Fig. 8). The OCV increases with the adding of Na amount. The theoretical electromotive force of a single cell is not influenced by the electrode materials. However, the OCV of a real cell is closely related to the kinetics of the charge transfer process in electrode reactions. As shown in Fig. 6, there are inert and insulated impurities such as $Sr_2Fe_2O_5$, $SrCO_3$ and $SrMoO_4$ in SFMN treated with wet CH_4, leading to the slowest charge transfer process and the lowest OCV of the single cell. Those impurities are decreased or disappeared with the increase of the amount of Na, which may accelerate the charge transfer process in the anode, and thus result in the

increase of OCV of the cell. However, the P_{max} of the single cell is influenced not only by the charge transfer process in the anode, but by the diffusion of active oxygen in the anode as well. As shown in Fig. S5, the oxygen vacancy concentration on the surface of SNa0.1FMN is much higher than that on the surface of SNa0.2FMN in wet CH_4 atmosphere, bringing about a faster anode reaction and a higher P_{max} of the single cell. The cells with SFMN, $SNa_{0.05}FMN$, $SNa_{0.1}FMN$ and $SNa_{0.2}FMN$ anodes reach P_{max} of 250, 450, 627 and 430 mW cm^{-2}, respectively. The P_{max} of the cell with $SNa_{0.1}FMN$ anode reaches 360 and 200 mW cm^{-2} at 800 and 750 ^{o}C, respectively (Fig. S6), and that cell exhibits stable power output for about 10 h at 850 ^{o}C with both H_2 and wet CH_4 as fuels (Fig. S7). Those results indicate that the doping of Na is a promising strategy for the design of novel anode materials with high electrochemical activity and high resistance to coking.

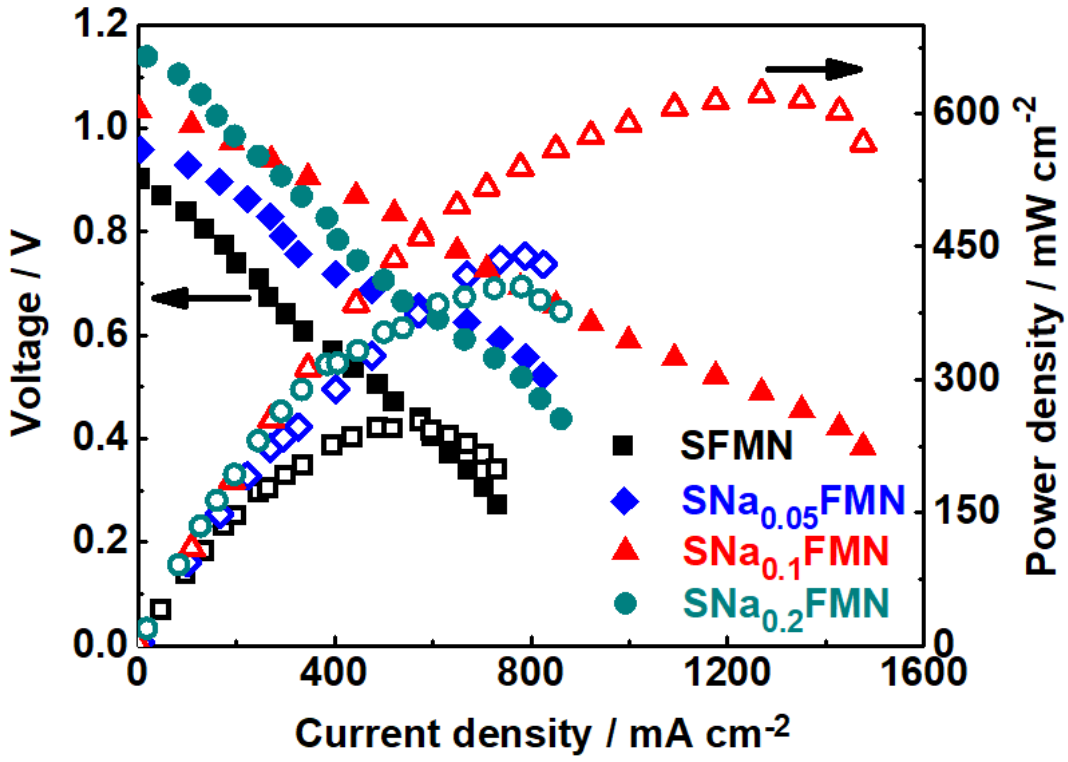

Fig. 8. *I-V* and *I-P* curves of the single cells with various anodes at 850 °C with wet CH_4 as fuel.

4. Conclusions

In this work, Na doped $Sr_2FeMo_{0.65}Ni_{0.35}O_{6-\delta}$ is investigated as an anode material for SOFCs with H_2 and CH_4 fuels. SFMN shows a pure perovskite structure in an oxidizing atmosphere, and $SrMoO_4$ and NiO impure phases are formed with the doping of Na. After reduction, phase transition from the perovskite to a RP structure is observed when the content of Na is less than 0.1, while $SNa_{0.2}FMN$ remains the perovskite phase without other oxide impurities. $FeNi_x$ alloy nanoparticles are formed on the surface of the anode powders after reduction, and the content of Ni in the

nanoparticles increases with the rise of the Na doping amount. The surface oxygen vacancy concentration increases slightly with the rise of Na content from 0 to 0.1, and then decreases significantly when the amount of Na reaches 0.2. $SNa_{0.1}FMN$ anode shows the highest activity mainly due to the acceleration of surface processes, and the single cell with that anode exhibits P_{max} of 1495 and 627 mW cm^{-2} at 850 ºC with H_2 and wet CH_4 as fuels, respectively. The coking resistance of the anode in CH_4 is also improved with Na doping.

Acknowledgments

The financial support of NSF of China under contract number 51402210 and the support of Tianjin Municipal Science and Technology Commission under contract number 15JCQNJC06500 are gratefully acknowledged. The work has been also supported by the Program of Introducing Talents to the University Disciplines under file number B06006, and the Program for Changjiang Scholars and Innovative Research Teams in Universities under file number IRT 0641.

Reference

[1] O. Yamamoto, Electrochim. Acta 45 (2000) 2423-2435.
[2] B.C.H. Steele, A. Heinzel, Nature 414 (2001) 345-352.
[3] Y.H. Huang, R.I. Dass, Z.L. Xing, J.B. Goodenough, Science 312 (2006) 254-257.
[4] B.A. Boukamp, Nat. Mater. 2 (2003) 294-296.
[5] G. Xiao, Q. Liu, F. Zhao, L. Zhang, C. Xia, F. Chen, J. Electrochem. Soc. 158 (2011) B455-B460.
[6] S. Kim, C. Kim, J.H. Lee, J. Shin, T.-H. Lim, G. Kim, Electrochim. Acta 225 (2017) 399-406.
[7] E. Nikolla, J. Schwank, S. Linic, J. Electrochem. Soc. 156 (2009) B1312-B1316.
[8] O.A. Marina, C. Bagger, S. Primdahl, M. Mogensen, Solid State Ionics 123 (1999) 199-208.
[9] S. Zha, Z. Cheng, M. Liu, Solid-State Lett. 8 (2005) A406-A408.
[10] A. Lashtabeg, J. Canales-Vazquez, J.T.S. Irvine, J.L. Bradley, Chem. Mater. 21 (2009) 3549-3561.
[11] M.A. Pena, J.L.G. Fierro, Chem. Rev. 101 (2001) 1981-2017.
[12] T. Inprasit, S. Wongkasemjit, S.J. Skinner, M. Burriel, P. Limthongkul, RSC Adv. 5 (2015)

2486-2492.
[13] G. Xiao, S. Nuansaeng, L. Zhang, S. Suthirakun, A. Heyden, H.-C. zur Loye, F. Chen, J. Mater. Chem. A 1 (2013) 10546-10552.
[14] Y. Song, Q. Zhong, W. Tan, C. Pan, Electrochim. Acta 139 (2014) 13-20.
[15] S.W. Tao, J.T.S. Irvine, Nat. Mater. 2 (2003) 320-323.
[16] D. Neagu, J.T.S. Irvine, Chem. Mater.22 (2010) 5042-5053.
[17] X.M. Ge, S.H. Chan, J. Electrochem. Soc.156 (2009) B386-B391.
[18] Z. Wang, Y. Tian, Y. Li, J. Power Sources 196 (2011) 6104-6109.
[19] H. Li, Y. Zhao, Y. Wang, Y. Li, Catal. Today 259 (2016) 417-422.
[20] S. Sengodan, S. Choi, A. Jun, T.H. Shin, Y.-W. Ju, H.Y. Jeong, J. Shin, J.T.S. Irvine, G. Kim, Nat. Mater. 14 (2015) 205-209.
[21] J.T.S. Irvine, D. Neagu, M.C. Verbraeken, C. Chatzichristodoulou, C. Graves, M.B. Mogensen, Nat. Energy 1 (2016) 15014.
[22] T. Zhu, H.E. Troiani, L.V. Mogni, M. Han, S.A. Barnett, Joule 2 (2018) 478-496.
[23] D. Neagu, T.-S. Oh, D.N. Miller, H. Menard, S.M. Bukhari, S.R. Gamble, R.J. Gorte, J.M. Vohs, J.T.S. Irvine, Nat. Commun. 6 (2015) 8120.
[24] C. Yang, J. Li, Y. Lin, J. Liu, F. Chen, M. Liu, Nano Energy 11 (2015) 704-710.
[25] C. Yang, Z. Yang, C. Jin, G. Xiao, F. Chen, M. Han, Adv. Mater. 24 (2012) 1439-1443.
[26] Z. Du, H. Zhao, S. Yi, Q. Xia, Y. Gong, Y. Zhang, X. Cheng, Y. Li, L. Gu, K. Swierczek, Acs Nano, 10 (2016) 8660-8669.
[27] O. Kwon, S. Sengodan, K. Kim, G. Kim, H.Y. Jeong, J. Shin, Y.-W. Ju, J.W. Han, G. Kim, Nat. Commun. 8 (2017) 15967.
[28] S.-e. Hou, J. Antonio Alonso, J.B. Goodenough, J. Power Sources 195 (2010) 280-284.
[29] S.-e. Hou, A. Aguadero, J. Antonio Alonso, J.B. Goodenough, J. Power Sources 196 (2011) 5478-5484.
[30] D. Neagu, G. Tsekouras, D.N. Miller, H. Ménard, J.T.S. Irvine, Nat. Chem. 5 (2013) 916.
[31] L. Kong, B. Liu, J. Zhao, Y. Gu, Y. Zhang, J. Power Sources 188 (2009) 114-117.
[32] N. Dai, J. Feng, Z. Wang, T. Jiang, W. Sun, J. Qiao, K. Sun, J. Mater. Chem. A 1 (2013) 14147-14153.
[33] J. Feng, J. Qiao, W. Wang, Z. Wang, W. Sun, K. Sun, Electrochim. Acta 215 (2016) 592-599.
[34] Z.P. Shao, W.S. Yang, Y. Cong, H. Dong, J.H. Tong, G.X. Xiong, J. Membr. Sci. 172 (2000) 177-188.
[35] Z.P. Shao, S.M. Haile, Nature, 431 (2004) 170-173.
[36] H. Sato, S.-i. Hashimoto, T. Nakamura, K. Yashiro, K. Amezawa, T. Kawada, ECS Trans. 57 (2013) 1125-1133.
[37] R.D. Shannon, Acta Cryst. A 32 (1976) 751-767.
[38] P.I. Cowin, R. Lan, C.T.G. Petit, H. Wang, S. Tao, J. Mater. Sci. 51 (2016) 4115-4124.
[39] L. Zhang, Q. Zhou, Q. He, T. He, J. Power Sources 195 (2010) 6356-6366.
[40] J. Harris, S. Andersson, Phys. Rev. Lett. 55 (1985) 1583-1586.
[41] G.A. Somorjai, Catal. Rev. 19 (1979) 105-159.
[42] F. Frusteri, F. Arena, G. Calogero, T. Torre, A. Parmaliana, Catal. Commun. 2 (2001) 49-56.
[43] F. Arena, F. Frusteri, A. Parmaliana, Appl. Catal. A 187 (1999) 127-140.
[44] A. Ponomareva, V. Babushok, E. Simonenko, N. Simonenko, V. Sevast'janov, O. Shilova, I. Kruchinina, J. Sol-Gel Sci. Technol. 87 (2018) 74-82.

Supplementary Materials

Enhanced activity and stability of $Sr_2FeMo_{0.65}Ni_{0.35}O_{6-\delta}$ anode for solid oxide fuel cells with Na doping

Tongtong Yao, Nianjun Hou, Juanjuan Gan, Jun Wang, Xiaojing Zhi, Lijun Fan, Tian Gan, Yicheng Zhao*, Yongdan Li

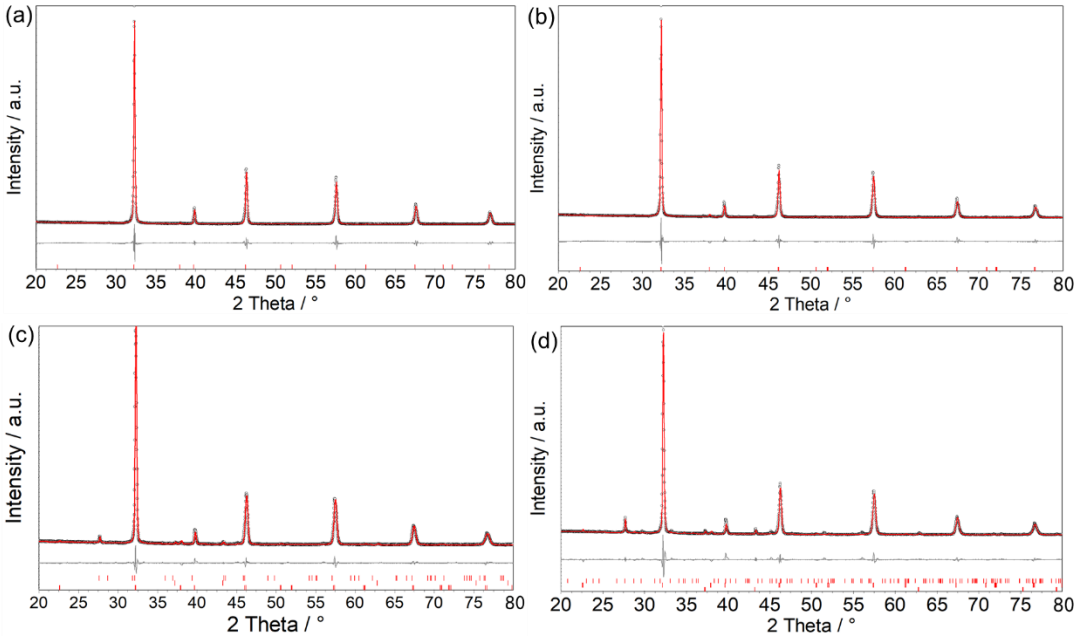

Fig. S1. Rietveld refinement of XRD patterns of different anodes before reduction. (a) SFMN; (b) $SNa_{0.05}FMN$; (c) $SNa_{0.1}FMN$ and (d) $SNa_{0.2}FMN$.

Table S1. Lattice parameters of the anode powders before reduction and fitting parameters of Rietveld refinement of the XRD patterns.

	SFMN	$SNa_{0.05}FMN$	$SNa_{0.1}FMN$	$SNa_{0.2}FMN$
Space group	*I* 4/*m*	*I* 4/*m*	*I* 4/*m*	*I* 4/*m*
a / Å	5.5484(1)	5.5502(1)	5.5526(1)	5.5637(6)
c / Å	7.8467(2)	7.8601(2)	7.8779(2)	7.8528(0)
V / $Å^3$	241.56(1)	242.12(1)	242.88(1)	243.08(7)
R-pattern/ %	2.61	3.09	2.29	3.16
R-weighted pattern/ %	3.81	4.55	3.35	4.82
R-Bragg/ %	0.80	1.45	0.81	0.92

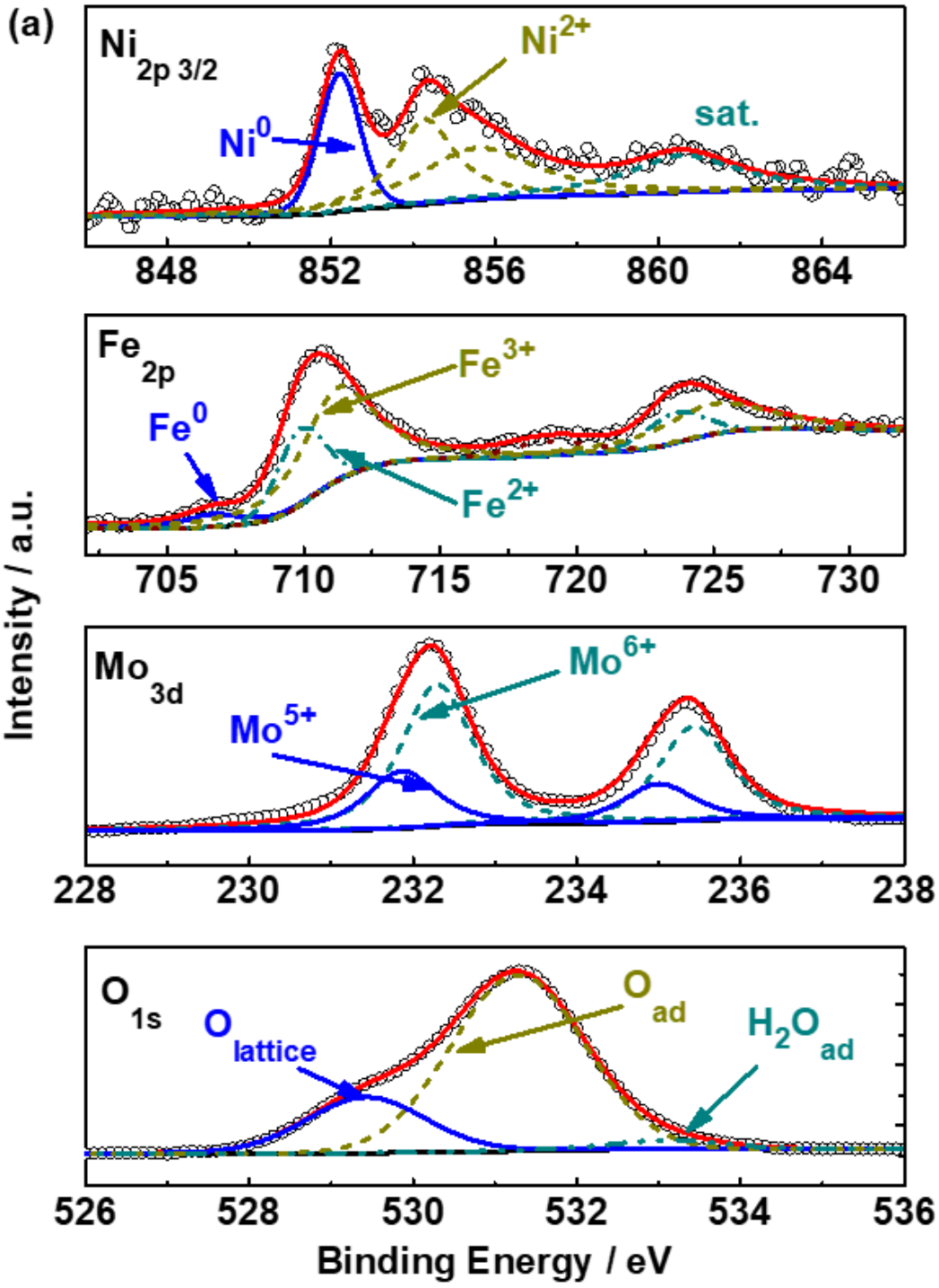
(a)
Ni 2p 3/2
Ni0
Ni2+
sat.
848
852
856
860
864
Fe 2p
Fe0
Fe3+
Fe2+
705
710
715
720
725
730
Mo 3d
Mo5+
Mo6+
228
230
232
234
236
238
O 1s
O lattice
O ad
H2O ad
526
528
530
532
534
536
Intensity / a.u.
Binding Energy / eV

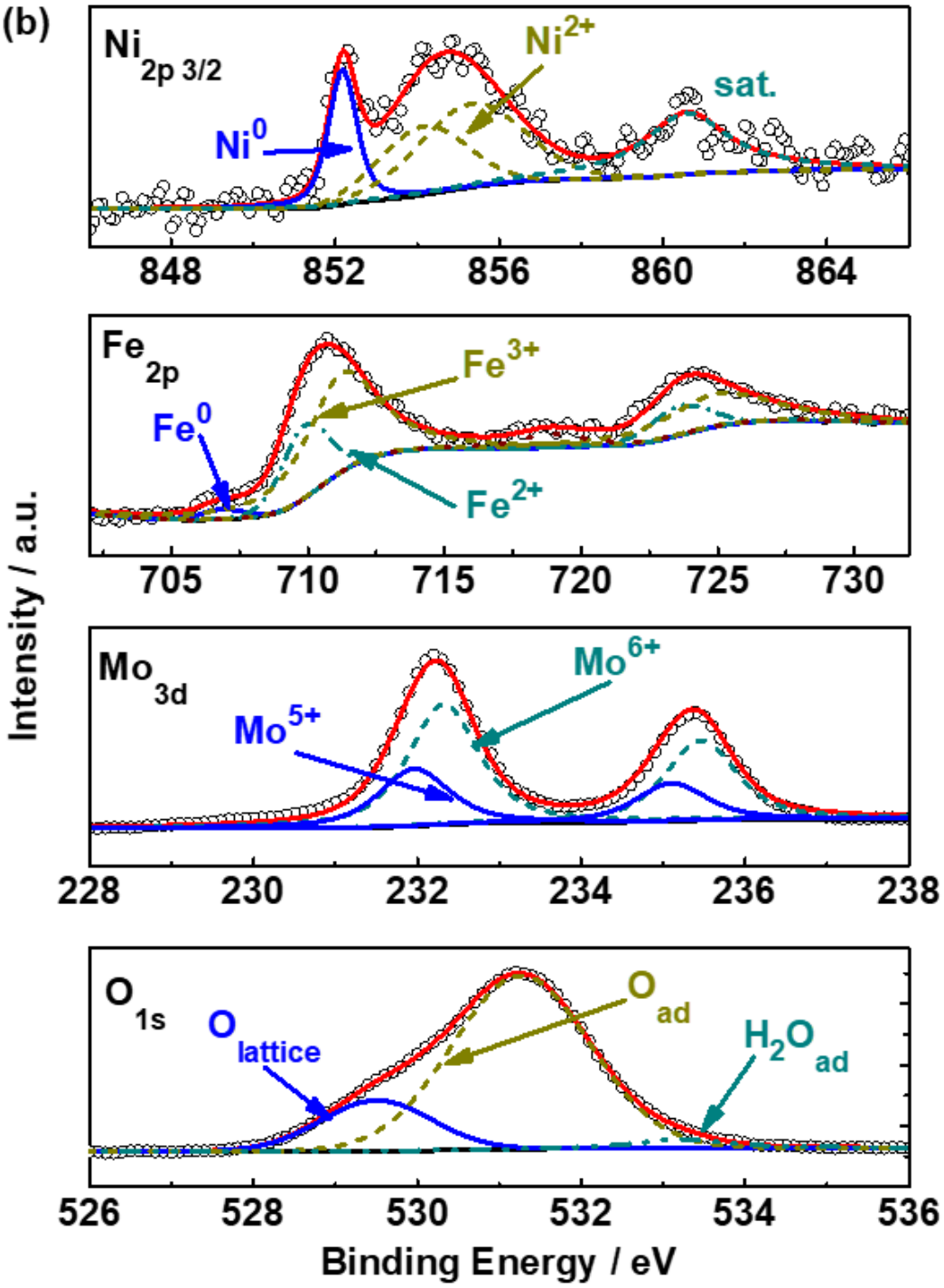
(b)
Ni 2p 3/2
Ni0
Ni2+
sat.
848
852
856
860
864
Fe 2p
Fe0
Fe3+
Fe2+
705
710
715
720
725
730
Mo 3d
Mo5+
Mo6+
228
230
232
234
236
238
O 1s
O lattice
O ad
H2O ad
526
528
530
532
534
536
Intensity / a.u.
Binding Energy / eV

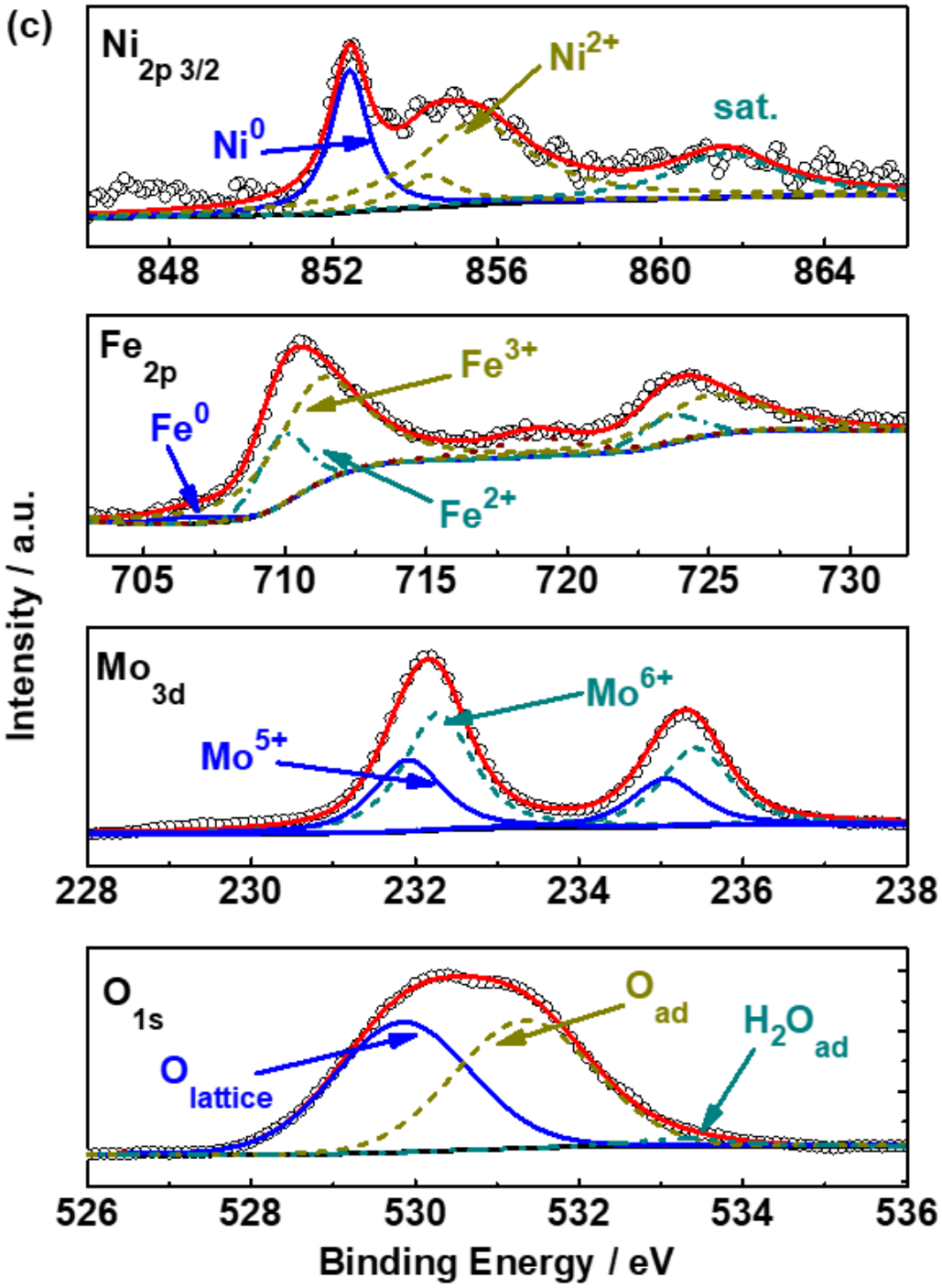

Fig. S2. XPS spectra of reduced (a) SFMN, (b) $SNa_{0.05}FMN$ and (c) $SNa_{0.2}FMN$ anode powders.

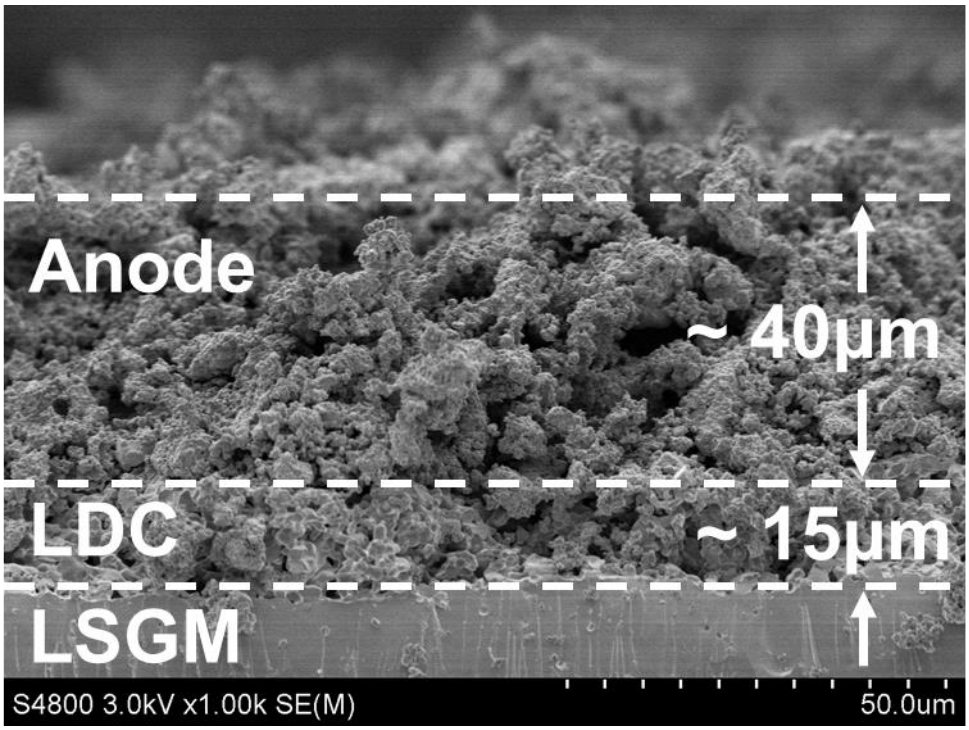

Fig. S3. Cross-sectional SEM image of the cell with $SN_{0.1}FMNi$ anode before test.

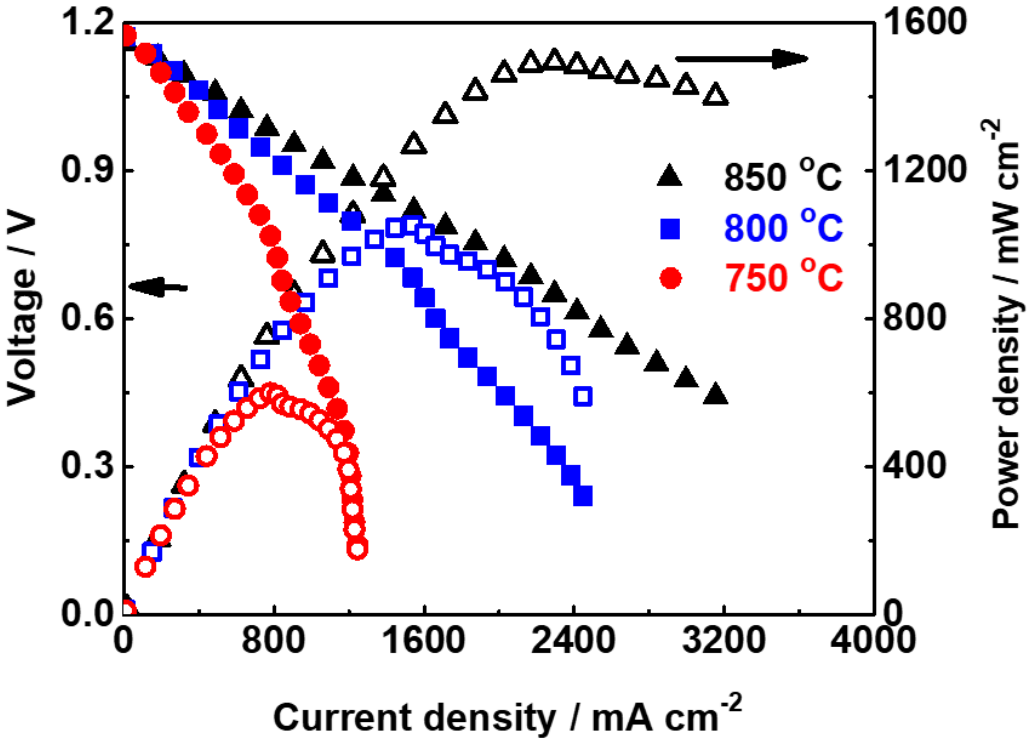

Fig. S4. *I-V* and *I-P* curves of the cell with $SNa_{0.1}FMN$ anode in 750-850 °C with dry H_2 as fuel.

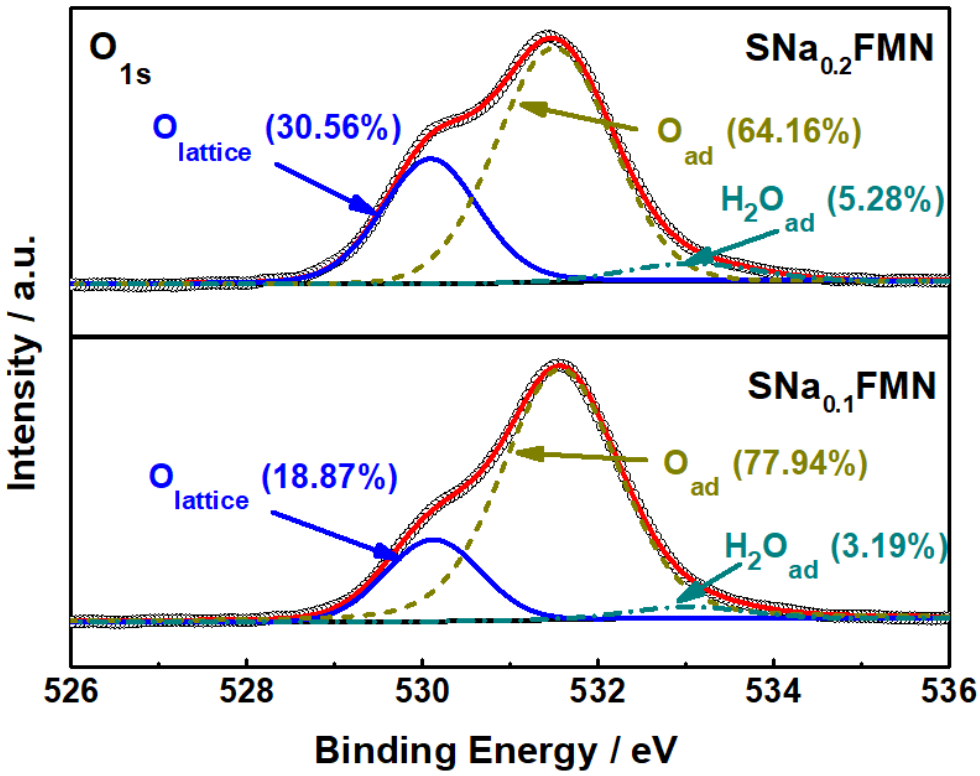

Fig. S5. O_{1s} XPS spectra of $SNa_{0.1}FMN$ and $SNa_{0.2}FMN$ anode powders treated in wet CH_4 after reduction.

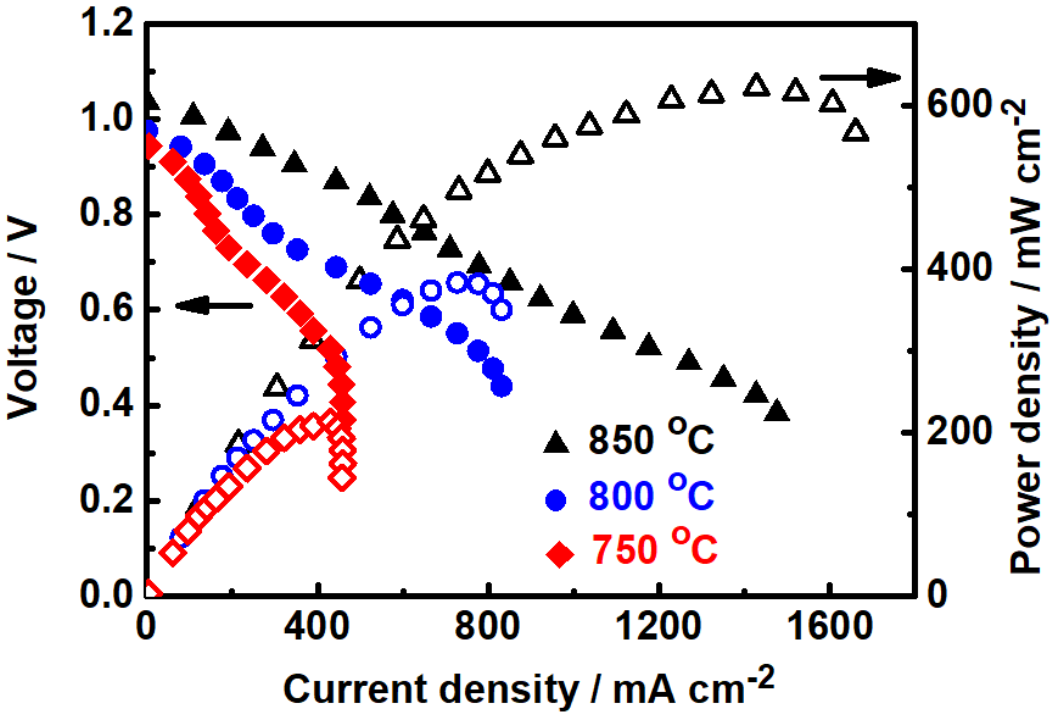

Fig. S6. *I-V* and *I-P* curves of the cell with $SNa_{0.1}FMN$ anode in 750-850 ºC with wet CH_4 as fuel.

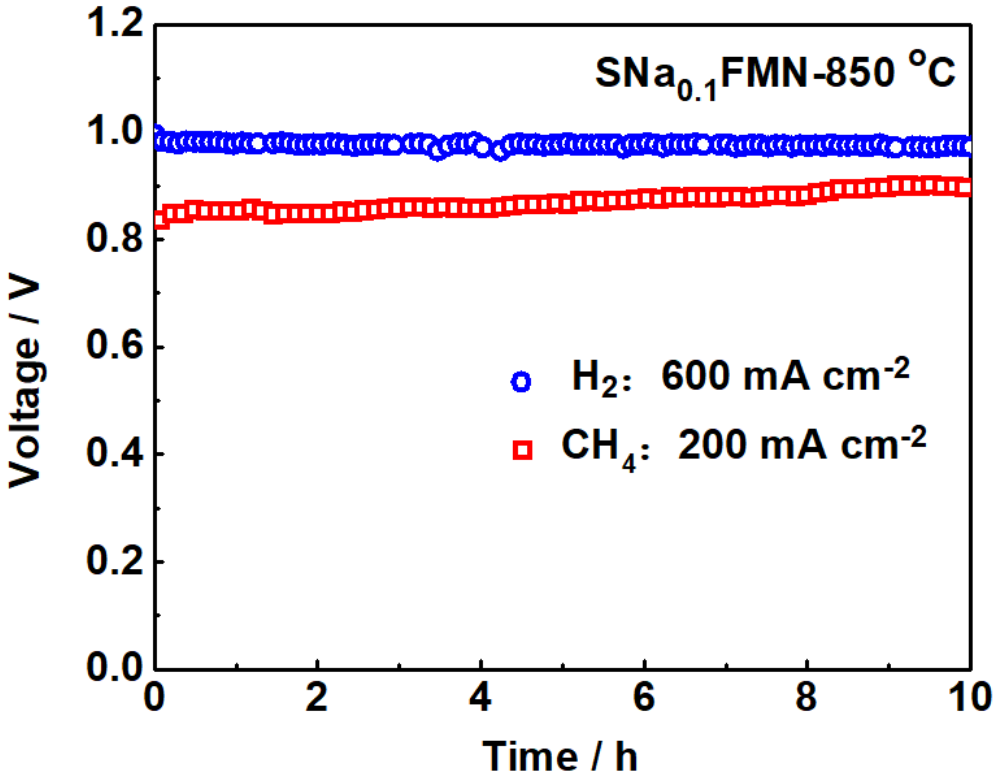

Fig. S7. Stability of the single cell with SNa0.1FMN as anode at 850 ºC using H_2 and CH_4 as fuels.